Chemical Engineering Journal 349 (2018) 708–718

Contents lists available at ScienceDirect

Chemical Engineering Journal

journal homepage: www.elsevier.com/locate/cej

Efficient adsorption and sustainable degradation of gaseous acetaldehyde and o-xylene using rGO-TiO_2 photocatalyst

Wenjiao Lin[a,b], Xiaofeng Xie[a,*], Xiao Wang[a], Yan Wang[a], Doris Segets[c], Jing Sun[a,*]

[a] Shanghai Institute of Ceramics, Chinese Academy of Sciences, 1295 Dingxi Road, Shanghai 200050, China
[b] University of Chinese Academy of Sciences, 19 (A) Yuquan Road, Beijing 100049, China
[c] Institute of Particle Technology (LFG), Friedrich-Alexander-Universität Erlangen-Nürnberg (FAU), 91058 Erlangen, Germany

HIGHLIGHTS

- rGO-TiO_2 for the photodegradation of two types of gaseous pollutants.
- The different adsorption and photodegradation mechanism of acetaldehyde and o-xylene.
- Different roles of $^{\cdot}O_2^-$ and $^{\cdot}OH$ in the process of photodegradation.
- Sustainable photodegradation of gaseous VOCs in a wide range of flow rates.

GRAPHICAL ABSTRACT

As-prepared rGO-TiO_2 nanocomposites exhibited superior adsorptivity and photodegradation ability in the degradation of acetaldehyde and o-xylene. Furthermore, this work firstly revealed the different roles of free radicals in the degradation of the two types of VOCs. $^{\cdot}O_2^-$ and $^{\cdot}OH$ played similar roles in the photocatalytic degradation process of o-xylene, while $^{\cdot}O_2^-$ was predominant radical in the degradation of acetaldehyde.

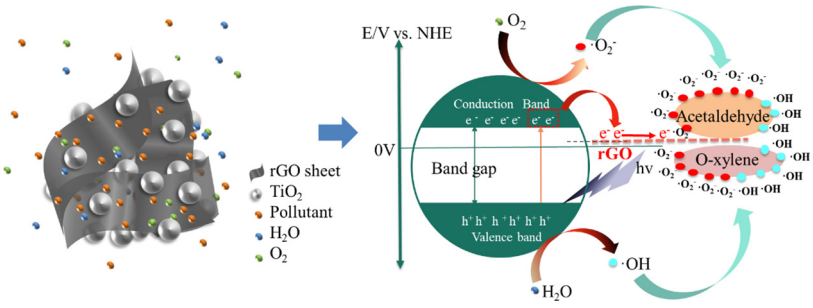

ARTICLE INFO

Keywords:
rGO-TiO_2
Photocatalysis
Acetaldehyde
O-xylene
VOCs removal

ABSTRACT

Two types of volatile organic chemicals (VOCs), acetaldehyde and o-xylene, were selected to probe the different adsorption and photodegradation mechanism of gaseous photocatalysis. Reduced graphene oxide (rGO)-TiO_2 nanocomposites were prepared by facile solvothermal process to perform the photocatalytic reactions. In the experiments, the removal efficiencies of the acetaldehyde and o-xylene at 80 mL·min^{-1} flow rate were only 15% and 12% when P25 was applied, while the efficiencies were sharply increased to 42% and 54% by using 0.5 wt% rGO-TiO_2 as the photocatalyst, respectively. Interestingly, it is notable that the removal efficiency of o-xylene was higher than that of acetaldehyde with identical rGO-TiO_2 photocatalyst. Experiments suggested that there were possibly two reasons. Firstly, the adsorbance of o-xylene was more than that of acetaldehyde owing to the π-π conjugation between rGO and aromatic compounds, which was proved by adsorption equilibrium and TPD tests. ESR tests proved that rGO can promote the generation of surface $^{\cdot}OH$ radicals and depress the $^{\cdot}O_2^-$ radicals formation. Compared with the dominant role played by $^{\cdot}O_2^-$ radicals in the degradation of acetaldehyde, an almost equal position of $^{\cdot}O_2^-$ and $^{\cdot}OH$ radicals was observed in the degradation of o-xylene according to the subsequent radical scavenger experiments. Moreover, the optimized rGO-TiO_2 exhibited sustainable photocatalytic activity at 40–120 mL·min^{-1} flow rate through 160 min tests, while P25 was deactivate

* Corresponding authors.
E-mail addresses: xxfshcn@163.com (X. Xie), jingsun@mail.sic.ac.cn (J. Sun).

https://doi.org/10.1016/j.cej.2018.05.107
Received 12 February 2018; Received in revised form 17 May 2018; Accepted 18 May 2018
Available online 19 May 2018
1385-8947/

only after 25 min. This work demonstrated the different adsorption and degradation characteristics of two types of VOCs, which could propel the target orientation design of photocatalyst in VOCs removal applications.

1. Introduction

Volatile organic chemicals (VOCs), which are detrimental to air quality and human health, have attracted increasing attention in recent years. Long-term exposure to VOCs will cause respiratory diseases, such as lung cancer [1]. In addition, VOCs can accelerate the formation of secondary organic aerosols that will turn into particles under oxidized conditions through complex heterogeneous reactions [2,3]. Several technologies have been applied for elimination of VOCs, including adsorption, bio-filtration, thermal catalysis, photocatalytic oxidation and so on [4–6]. Among these methods, photocatalysis is an effective technology since it is non-toxic, low-cost and capable of removing various gaseous pollutants under sunlight. Up to now, most reports focus on the photodegradation of single pollutant in water [7] and static gas [8]. Assadi and Bouzaza did some research about the photocatalytic oxidation of VOCs in a continuous flow mode and investigated the effect of different operating parameters [9–13]. However, there are various dynamic gaseous VOCs in the atmosphere, including alkene, aromatics, aldehyde, and so on. The different structures lead to the differences in the degradation mechanisms. To the best of our knowledge, reports about the difference between the photodegradation of different VOCs are still limited.

Titanium dioxide (TiO_2) is a promising photocatalyst that has been widely used in the photodegradation of different pollutants [14]. However, some intrinsic shortcomings of TiO_2 limit its practical application in the degradation of gaseous pollutants. Normally, TiO_2 shows weak adsorptivity for gaseous pollutants and high recombination rate of e^--h^+ pairs. Up to now, various strategies have been proposed to overcome these shortcomings. Zeolite, active carbon or other cellular materials were combined with TiO_2 in order to enhance its adsorption ability [15]. Doping or the combination with various semiconductors have been employed to inhibit the recombination of e^--h^+ pairs [16–18]. After coupling TiO_2 with other semiconductors, the charge carriers can be separated by interfacial transfer. Take the CdS-TiO_2 nanocomposite for example [19], the photon-induced electrons generated in CdS could transfer to the conduction band of TiO_2, while the photogenerated holes in TiO_2 accumulate in the valence band of CdS. Through combining various semiconductors, including ZnO [20], WO_3 [21], SnO_2 [22,23], $MnCO_3$ [24], Ag_3VO_4 [25], with TiO_2, enhanced photocatalytic activity in the degradation of VOCs have been achieved. However, these strategies cannot facilitate the separation of charge carriers and promote the adsorption ability simultaneously. Besides, photocatalysis is a complex heterogeneous reaction with various kinds of intermediates [26]. These intermediates will adsorb on the active sites at the surface of TiO_2, leading to the deactivation over time [26–30]. Regenerated by heating at high temperature or by exposure in clean air under UV light irradiation is possible, however needs a long period of time and extra cost. Therefore, multifunctional materials have to be identified to overcome these shortcomings simultaneously.

Graphene, a two dimensional material with large specific surface area and remarkable electron mobility, should be a good choice. When TiO_2 is combined with graphene, the photo-generated electrons in the valence band of TiO_2 can transfer to graphene, prolonging the lifetime of the photo-generated e^--h^+ pairs [31–33]. This is a major importance for the generation of different free radicals, which facilitate the oxidation of pollutants and intermediates, and thus prolong the lifetime of the photocatalyst. In addition, the π-conjugation structure on graphene will effectively facilitate the adsorption of gaseous organic pollutants, especially aromatics. Researchers have reported many methods to synthesize TiO_2-graphene composites [34–38]. These nanocomposites exhibited an improved photocatalytic efficiency in the degradation of pollutants in liquid phase, including methylene blue [39–41], rhodamine B [42], bisphenol A [43], acetic acid [44] methylene orange [38], malachite green [45], phenol solution [46], and others [47]. Besides, the group of Huang demonstrated that the composite material showed high photocatalytic activity during degradation of static gaseous formaldehyde [36]. The enhanced photocatalytic activity suggests that this composite is a promising material in the degradation of dynamic gaseous pollutants owing to its superior adsorptivity and excellent charge separation properties.

Herein, we report the synthesis of hybrids of rGO with TiO_2 prepared by a facile solvothermal process. The photocatalytic activity of as-prepared photocatalysts was evaluated by the photodegradation of low concentration (at ppm level) dynamic gaseous o-xylene and acetaldehyde. O-xylene is a typical industrial pollutant that contains a phenyl ring, while acetaldehyde is a common indoor air pollutant that contains an aldehyde group. After combining with rGO, the photocatalytic efficiency was significantly improved. The underlying causes of the improvement of the photocatalytic activity were further investigated by a series of characterizations. The differences between the adsorptivity for o-xylene and acetaldehyde were analyzed by temperature programmed desorption (TPD) and adsorption tests. Finally, ESR and radical scavengers were used for further investigating the roles of different active radicals and the mechanism of the photocatalytic reaction. Overall, this work provides a promising photocatalyst with promoted photocatalytic activity and demonstrates the different adsorption and photodegradation mechanism of types of VOCs.

2. Experimental

All chemical agents used in our study were of analytical grade and used without further purification. Tetrabutyl titanate and sulfuric acid were purchased from Sinopharm Chemical Reagent CO., Ltd. Ethanol absolute was supplied by Shanghai zhenxing CO., Ltd. Deionized (DI) water was produced by a Milli-Q system (R > 18.1 MΩ).

2.1. Preparation of samples

GO was synthesized by a modified Hummer's method [48–50] and the nanocomposites were synthesized by a facile solvothermal treatment. In a typical preparation process, 5.0 g of tetrabutyl orthotitanate was added to a round bottom flask containing 400 mL absolute ethanol. 4 mL deionized water was dropwise added into the solution, followed by refluxing at 351 K for 6 h. The as-prepared amorphous TiO_2 was washed three times with deionized water and absolute ethanol. Then the TiO_2 was isolated by centrifugalization. An appropriate amount of GO and amorphous TiO_2 were dispersed into the mixture of 50 mL H_2O and 25 mL ethanol, inside the pH was adjusted to 4 by adding a few drops of dilute sulfuric acid. After being ultrasonicated for 1 h, the suspension was stirred for further 2 h to obtain a homogeneous suspension. Then the suspension was placed in a Teflon-lined stainless steel autoclave (Volume 100 mL) and kept at 433 K for 6 h. The products were defined as xwt% rGO-TiO_2, in which xwt% represents the mass ratio of rGO to TiO_2. For comparison, the mixture of GO sheets and amorphous TiO_2 particles that has not been treated by a solvothermal process after intimate mixing of the two materials was defined as xwt% GO-TiO_2. Pure TiO_2 was prepared by the same solvothermal treatment in the absence of GO.

2.2. Characterization

Transmission electron microscopy (TEM, JEM-2100F) was applied to characterize the microstructure and morphology. The X-ray diffraction (XRD) spectra were recorded using an X-ray diffractometer (Ultima IV 2036E102, Rigaku Corporation, Japan). Raman spectra were recorded using a DXR Raman Microscope (Thermal Scientific Corporation, USA). X-ray photoelectron spectroscopy (XPS) analysis was carried out using a Microlab 310F scanning Auger microprobe (VG Scientific Ltd). The JES-FA200 spectrometer was applied to record the electron spin resonance (ESR) signals of radicals. 5,5-dimethyl-1-pyrroline N-oxide (DMPO) was used as radicals trapper. Photoluminescence (PL) spectra were recorded by an Edinburgh FL/FS900 spectrophotometer with an excitation wavelength of 320 nm. TPD analyses were performed using a ChemiSorb PCA-1200 (Builer, China). During the test, 0.05 g of the sample was placed in a quartz tube inside an electric furnace, heated at 393 K for 1 h in high-purity nitrogen gas in order to remove the adsorbed organics and hydrates. After cooling to room temperature, acetaldehyde (or o-xylene, respectively) was introduced into the tube at a flow rate of 30 mL·min^{-1} for 2 h to reach the adsorption equilibrium. Then high purity nitrogen was introduced into the tube and the temperature was raised at a ramp of 10 K·min^{-1} to detect the desorption process of acetaldehyde (or o-xylene).

2.3. Adsorption and photocatalytic performance

Both of the adsorption and photodegradation tests were carried out in a real-time monitoring system (Scheme 1). The real-time monitoring system contains a gas mixer, a reaction cell and a gas chromatograph (GC). The reaction cell contains a rectangular chamber (20 cm × 10 cm × 1.5 cm) and a 200 W Xenon lamp that is 30 cm above the chamber. During the test, 0.1 g photocatalyst, which was uniformly coated on the glass pane with a surface area of 60 cm^2, was placed in the chamber and sealed with a quartz glass. The gaseous VOCs mixed with dried air in the mixer. The mixed gas could flow into the GC through valve 3 and valve 4 before starting the test and the concentration of acetaldehyde or o-xylene can be detected by the FID detector of GC. The concentration kept at 25 ppm for all experiments. During the adsorption and photodegradation tests, the mixed gas flowed into the reaction cell through valve 3 and contacted with the photocatalyst in the rectangular chamber. Then the residual gas in the chamber will flow into GC through valve 5 and valve 4 to determinate the concentration of the pollutants.

The adsorption capacity of the nanocomposite was tested in the dark. The gaseous pollutants (acetaldehyde or o-xylene) was fed into the chamber at a flow rate of 10 mL·min^{-1} until an adsorption equilibrium was achieved. Eq. (1) calculated the value of saturated adsorbance (V (mL), which indicates the volume of the gas that containing 25 ppm of acetaldehyde or o-xylene). ν (mL·min^{-1}) is the volume flux of the gaseous pollutants. C_0 and C (ppm) are the concentrations of the reaction gas at the inlet and outlet of the chamber, respectively. T (min) is the equilibrium time. The first part in the equation is the definite integral of the adsorption curve for the as-prepared material. The second part is the definite integral of the curve for the blank experiment.

$$V=\left[\int_0^T \nu\times(1-C/C_0)dt\right]_{sample}-\left[\int_0^T \nu\times(1-C/C_0)dt\right]_{blank} \quad (1)$$

After reaching the adsorption equilibrium, the Xenon lamp was turned on to test the photocatalytic activity. All tests were performed at room temperature and atmospheric pressure. The relative humidity was 60%. Eq. (2) calculated the removal efficiency Y:

$$Y=(C_0-C)/C_0\times 100\% \quad (2)$$

3. Results and discussion

3.1. Characterization of photocatalysts

First, the morphology of GO, pure TiO_2, and 0.5 wt%rGO-TiO_2 was observed by TEM. From the low magnification images (Fig. 1a–c), the size of GO was determined to be about several microns, while typical diameters of pure TiO_2 particles were about 8–10 nm. The rGO sheet in the composites retained the two-dimensional structure with wrinkles. From the high resolution image shown in Fig. 1d, rGO sheets wrapped the TiO_2 particles in the as-prepared nanocomposites, which is meaningful to optimize the adsorptivity of the material. As mentioned, GO and TiO_2 were mixed in an acidic solution during the final step of our preparation process. The zeta (ζ) potential of TiO_2 particles was positive, while the surface of the GO sheets was negatively charged. The resulting electrostatic attraction facilitated the assembly of GO and TiO_2. Besides, the fringes spacing was found to be 0.35 nm, which can be ascribed to the (1 0 1) crystal facet of anatase.

The phase structure was characterized by XRD (Fig. 2a). In line with the expectation from HRTEM, the diffraction peaks in XRD patterns are typical for crystal planes of anatase TiO_2 (JCPDS PDF#: 00-021-1272). The analogous patterns of as-prepared nanocomposites and pure TiO_2 indicate that rGO has little influence on the crystallinity of the TiO_2 nanoparticles. No typical peak of graphene was observed because of its low content in the nanocomposite materials. The samples were also characterized by Raman spectroscopy (Fig. 2b–d). The four bands at low frequencies (100–650 cm^{-1}) are typical peaks reported for anatase TiO_2 (Fig. 2c). After combining TiO_2 with rGO, the peaks at 403.4, 518.2 and 640.5 cm^{-1} down-shifted to 398.8, 514.5 and 639.8 cm^{-1}, respectively. The peaks around 403.4 and 640.5 cm^{-1} represent the stretching vibration of the O—Ti—O bond. The peak around 514.5 cm^{-1} represents the bending vibration of Ti—O—Ti bond [51]. The red shift indicates a lengthening of the Ti–O bond because of the formation of Ti—O—C bond between rGO sheets and TiO_2 particles. In addition, the two bands located at 1351 and 1600 cm^{-1} (Fig. 2d) are the D and G band of graphene, respectively. The D band is usually associated with the sp^3 defects, while the G band corresponds to the vibration of the sp^2 hybridization [52,53]. Accordingly, the intensity ratio of D to G band (I_D/I_G) is a measure of the relative ratio of local defects (or disorders) to the sp^2 hybridized graphene domains. It has been reported that the reduction process leads to a decrease of sp^2 hybridization, inducing an increase in the I_D/I_G ratio [54–57]. As shown in Table 1, the value of I_D/I_G increased from 0.87 to 0.98 upon solvothermal treatment, confirming the efficient reduction of GO.

In the next step, XPS was applied to further investigate the chemical status of the atoms in 0.5 wt% GO-TiO_2 and 0.5 wt% rGO-TiO_2. As shown by the XPS spectra (Fig. 3a and b), the chemical binding energies around 458.6 eV (Ti $2p_{3/2}$), 523.0 eV (O 1s), and 285 eV (C 1s) are characteristic for Ti, O and C elementals, respectively. The C_{1s} XPS

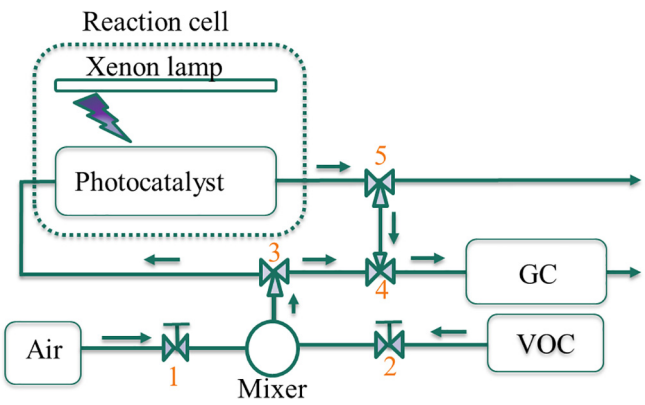

Scheme 1. Real-time monitoring system.

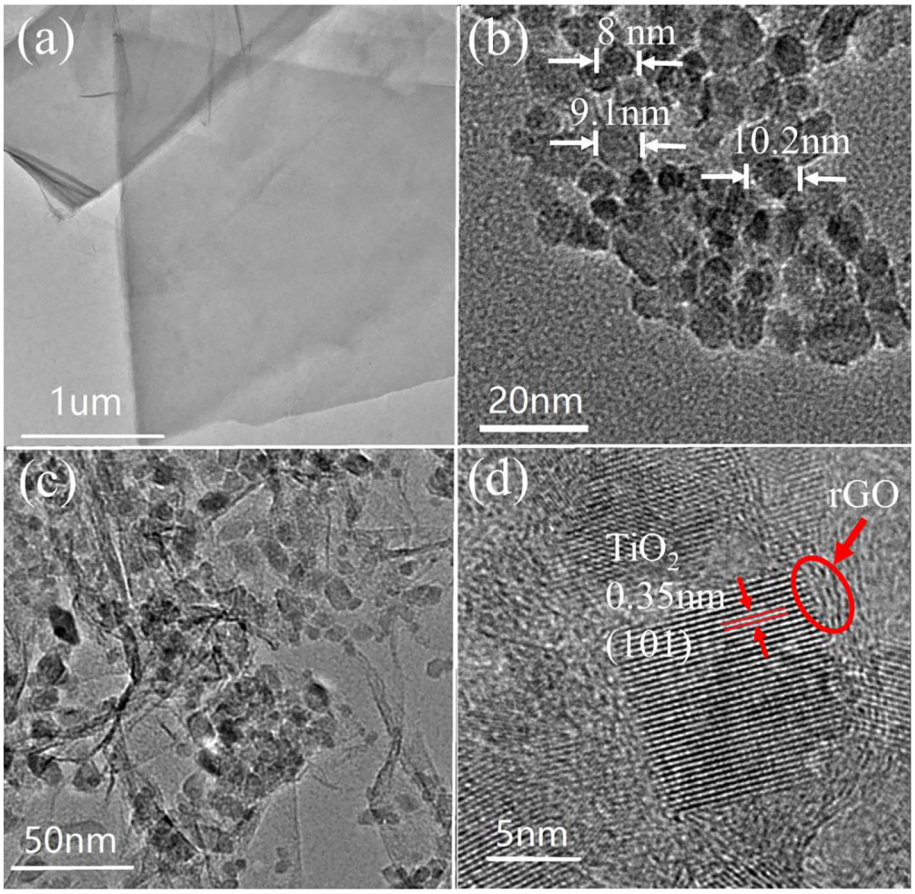

Fig. 1. TEM images of (a) GO, (b) pure-TiO_2 and (c) 0.5 wt% rGO-TiO_2; HRTEM image of (d) 0.5 wt% rGO-TiO_2.

spectra were deconvoluted into three peaks. As shown in Fig. 3c and d, the peaks around 285 eV, 286.6, and 289.2 eV are typical peaks for the C═C, C—O and C═O bonds, respectively. For comparison, the relative proportion of oxygen-containing species and the atomic ratio of O/C were calculated according to the XPS spectra. As shown in Table 1, the relative proportion of oxygen-containing species and the atomic ratio of O/C in the composite decreased after solvothermal treatment, indicating again the effective reduction of GO nanosheets. Additionally, the proportion of the C═C bond increased from 50.4% to 75.9% after reduction. This suggests that the sp^2 bonded C atoms were restored during the solvothermal treatment [58]. This restoration of C═C bond can improve the conductivity of GO, which is important for the efficient electron transfer.

3.2. Enhanced photocatalytic activity

The influence of the rGO content on the photocatalytic activity was evaluated by the degradation of o-xylene and acetaldehyde at a flow rate of 80 mL·min^{-1}, respectively. Adsorption equilibrium was first reached before the photocatalytic process. Fig. 4a showed the degradation result of o-xylene under UV light irradiation. Compared with pure TiO_2, the composite materials exhibited a clearly enhanced photocatalytic activity. The final photocatalytic efficiency first increased with higher rGO content, followed by a decrease when the rGO mass ratio exceeded 0.5 wt%. Thus 0.5 wt% rGO-TiO_2 exhibited an optimum activity with a photocatalytic efficiency of 54%. Noteworthy, in our reference experiments, this was found to be 4.5 times higher than the photocatalytic efficiency of P25 (12%) and 1.8 times higher than the efficiency of pure TiO_2 synthesized under solvothermal conditions (30%). A similar result was found for the degradation of acetaldehyde, which is shown in Fig. 4b. The photocatalytic efficiency was about 15% with P25 and 28% with pure TiO_2. In contrast, the optimum hybrid material, 0.5 wt% rGO-TiO_2 exhibited the highest photocatalytic efficiency of 42%, and thus 2.7 times as high as P25 and 1.4 times as high as pure TiO_2. Again, a further increase of the rGO content (over 0.5 wt %) caused a decrease in the photocatalytic efficiency. These results indicate that the moderate addition of rGO can substantially facilitate the photodegradation of dynamic gaseous o-xylene and acetaldehyde. It is worth mentioning that the removal efficiency of o-xylene was higher than that of acetaldehyde with identical as-prepared composite material (Fig. 4c), while the removal efficiency of acetaldehyde was a little higher than that of o-xylene with P25. Besides, the photocatalytic efficiency of 2 wt% rGO-TiO_2, which was higher than that of pure TiO_2 in the degradation of o-xylene, was lower than that of pure TiO_2 in the degradation of acetaldehyde. It indicated that the rGO-TiO_2 photocatalysts were more suitable for the photodegradation of o-xylene, which will be discussed in the following.

The photocatalytic activity of 0.5 wt% rGO-TiO_2 as optimum hybrid material and P25 as technically relevant reference material were further investigated by the degradation of gaseous o-xylene at different flow rates. As shown in Fig. 5a and c, the photocatalytic efficiency of 0.5 wt% rGO-TiO_2 decreased from 63% to 53% when the flow rate increased from 40 mL·min^{-1} to 80 mL·min^{-1}. When the flow rate reached 120 mL·min^{-1}, the photocatalytic efficiency was 29%. In contrast, when P25 was applied (Fig. 5b and c), the photocatalytic efficiency was 15%, 10%, and 4% at a flow rate of 40 mL·min^{-1}, 80 mL·min^{-1}, and 120 mL·min^{-1}, respectively. The photocatalytic efficiency decreased significantly with increasing flow rate. It is easy to understand that polluted gases move faster at a high flow rate, thus the residence time of the pollutant molecules in the reaction chamber becomes shorter, resulting in strongly reduced contact (for adsorption) and reaction (for chemical conversion) times for the different gases with the

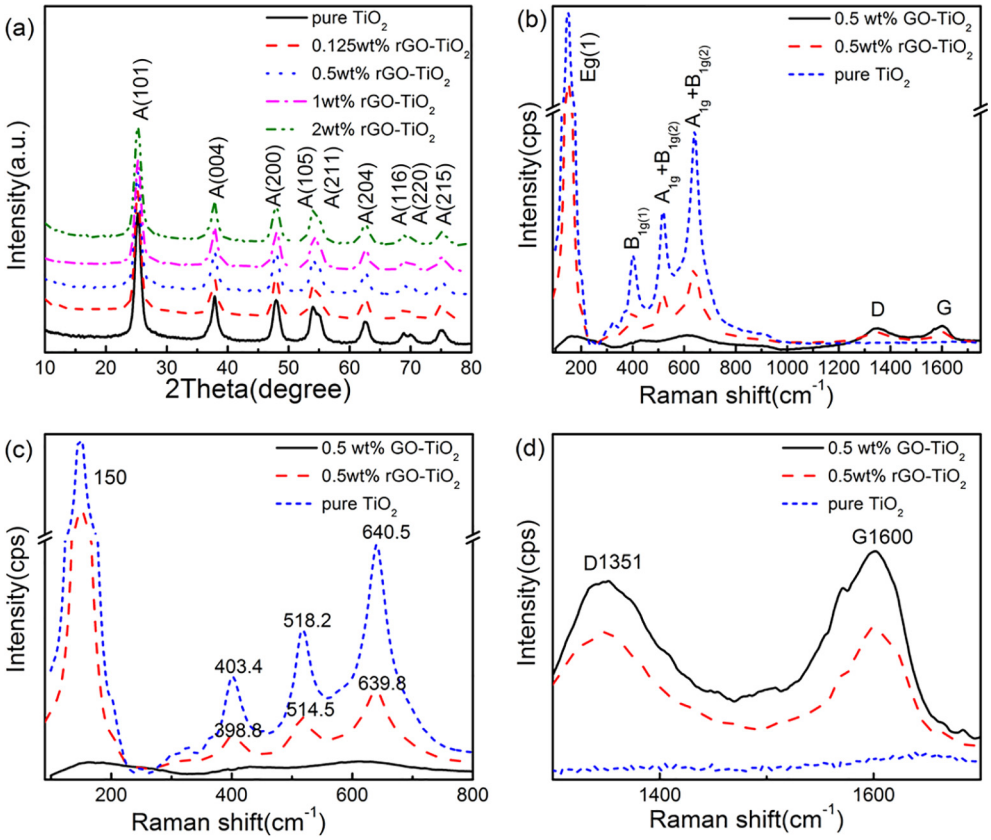

Fig. 2. (a) XRD patterns of pure TiO_2 and xwt% rGO-TiO_2; (b, c, d) Raman spectra of pure TiO_2, 0.5 wt% GO-TiO_2 and 0.5 wt% rGO-TiO_2.

Table 1
Structural properties of 0.5 wt% GO-TiO_2 and 0.5 wt% rGO-TiO_2 were characterized by Raman and XPS spectroscopy, respectively. (i) The I_D/I_G intensity ratio in Raman spectra. (ii) The relative proportion of different oxygen-containing species and the atomic ratio of O/C extracted from XPS spectra.

Samples	(i) Raman spectra	(ii) XPS spectra			
	I_D/I_G	C=C (%) 285(eV)	C–O (%) 286.5(eV)	C=O (%) 289.2(eV)	O/C
0.5 wt% GO-TiO_2	0.87	50.4	39.8	9.8	2.16
0.5 wt% rGO-TiO_2	0.98	75.9	18.8	5.3	1.35

photocatalysts under investigation. The degradation efficiency for dynamic gaseous pollutants was higher at lower flow rate due to the longer residence time, indicating that the photodegradation performance can be optimized by prolonging the residence time when we design the reactor in the practical application. Compared with P25, the as-prepared nanocomposite showed higher photocatalytic activity at all flow rates under investigation and the overall decrease was much more pronounced in case of P25 than in case of 0.5 wt% rGO-TiO_2. Moreover, the photocatalytic efficiency of the nanocomposite was stable during the whole test period lasting for 160 min, while that of P25 already decreased after 25 min. Besides, the photocatalysts (0.5 wt% rGO-TiO_2) could remain activity in the 3-times cyclic experiments for the photodegradation of gaseous o-xylene at different flow rate (Fig. S1). This indicates that the as-prepared nanocomposite is strongly superior to commercial P25 for the elimination of dynamic gaseous VOCs.

To explore the underlying causes of the improvement of the photocatalytic activity, a series of characterizations were carried out. Adsorption tests were performed to investigate the adsorptivity of the as-prepared composite materials for gaseous acetaldehyde and o-xylene. As shown in Fig. 6a and b, the concentration of o-xylene and acetaldehyde decreased immediately when the gas flow entered the reaction chamber. Parts of the o-xylene or acetaldehyde molecules adsorbed on the surface of the photocatalyst. With the continuous feed of replenishing gas, the concentration recovered until a final adsorption equilibrium was reached. According to Fig. 6a, at constant volume flow rate, the nanocomposite with higher rGO content took longer to reach the adsorption equilibrium. In the meantime, the reversal peak area of the adsorption curve increased with the rGO content, indicating that the composite materials with higher rGO content can adsorb more o-xylene molecules. Analogous conclusion can be drawn from Fig. 6b. The derived value of the saturated adsorbance (V) is equal to the difference between the reversal peak area of the blank curve and that of the adsorption curve for as-prepared nanocomposites, which was shown in Eq. (1). The reversal peak area of the adsorption curve was worked out with the theory of definite integral. As shown in Fig. 6c and d, the saturated adsorbance of o-xylene and acetaldehyde increased with rGO content and the amount of adsorbed gaseous acetaldehyde was less than that of gaseous o-xylene on the same composite material. Especially, the mass ratio of rGO has stronger influence on the adsorption property of o-xylene since the slope of o-xylene is greater than that of acetaldehyde. These phenomena are mainly due to the π-π conjugation between rGO sheet and o-xylene molecule.

The TPD tests were carried out to provide an insight into the interactions between the nanocomposite and o-xylene (or acetaldehyde). There were two distinguishable desorption peaks in the o-xylene-TPD (Fig. 7a). The weakly bound o-xylene desorbed at around 393 K and the strongly bound o-xylene desorbed at around 523 K. After combining TiO_2 with rGO, the area of both peaks increased, indicating that more o-xylene desorbed from the surface of the photocatalyst. Besides, the peaks shifted upward to the higher temperatures after the addition of rGO, indicating the stronger adsorption affinity for o-xylene molecules. A similar situation was found in the acetaldehyde-TPD (Fig. 7b). Thus, we can draw the conclusion that rGO effectively enhances the adsorptivity for o-xylene and acetaldehyde.

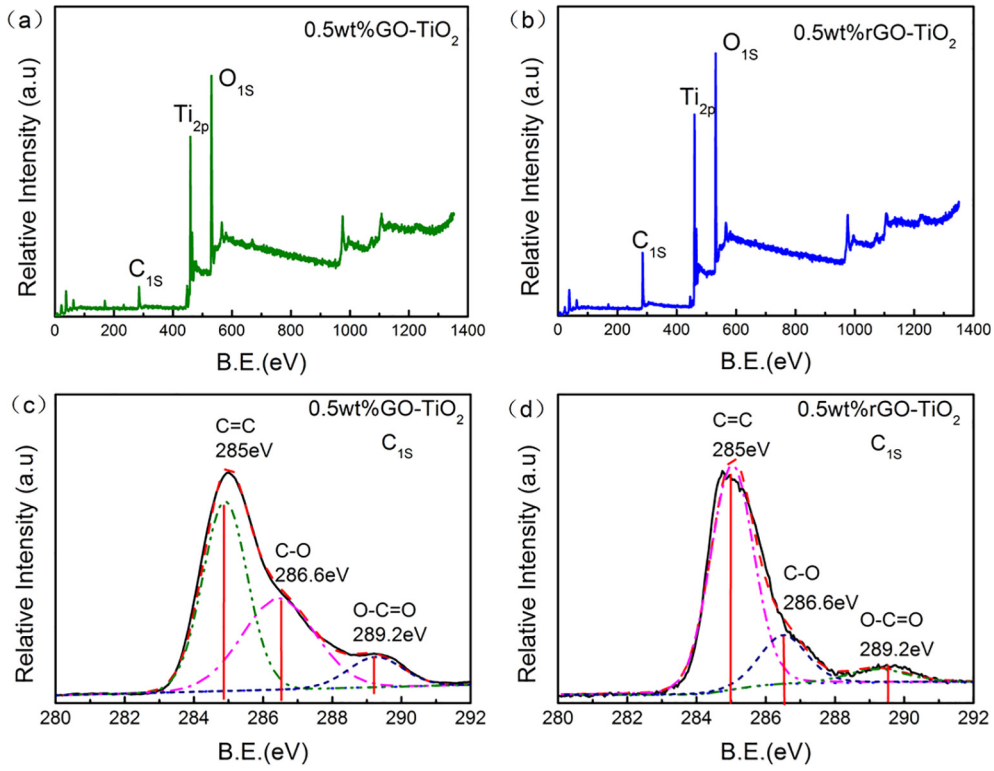

Fig. 3. The XPS survey spectra of (a) 0.5 wt% GO-TiO_2 and (b) 0.5 wt% rGO-TiO_2; the C 1s XPS spectra of (c) 0.5 wt% GO-TiO_2 (d) 0.5 wt% rGO-TiO_2.

The specific surface area was measured and the data were listed in Table S1. According to the Table S1, there was no noticeable difference in the specific surface area of pure TiO_2 and nanocomposites. It indicated that the improvement of the adsorption capacity for as-prepared nanocomposite was not caused by the changes in specific surface area. Adsorption is a complicated processes controlled by many other

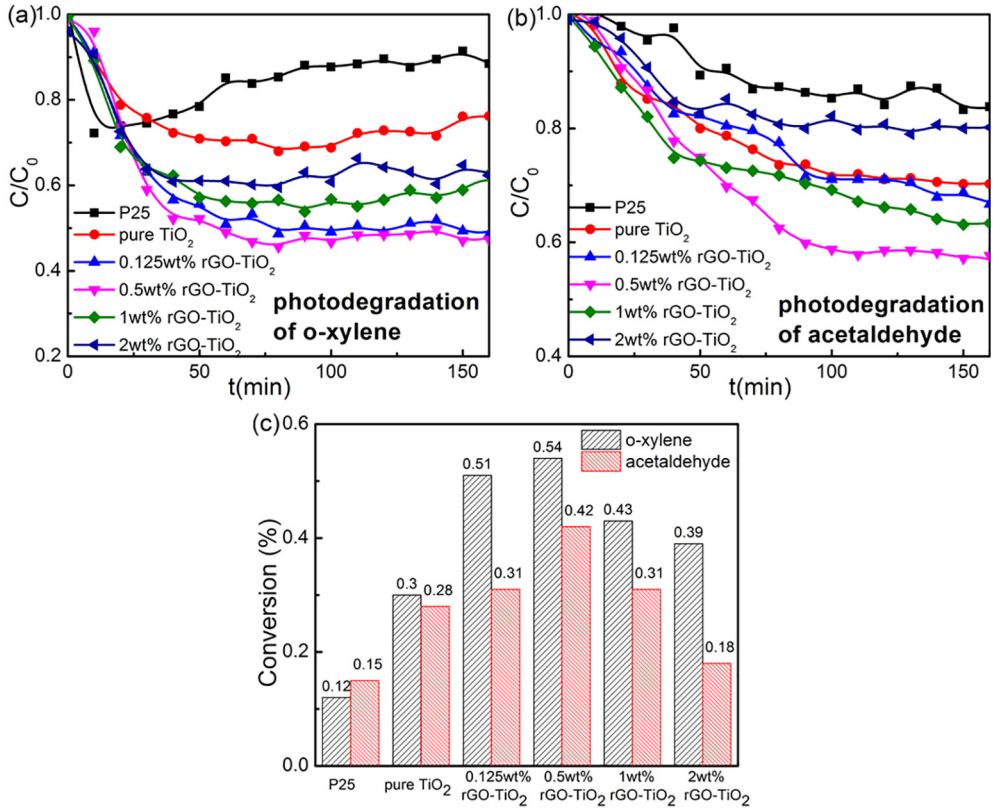

Fig. 4. Photocatalytic degradation of flowing mode gaseous (a) o-xylene and (b) acetaldehyde on different samples under UV light at a flow rate of 80 mL·min^{-1}; (c) comparison between removal efficiency of o-xylene and acetaldehyde.

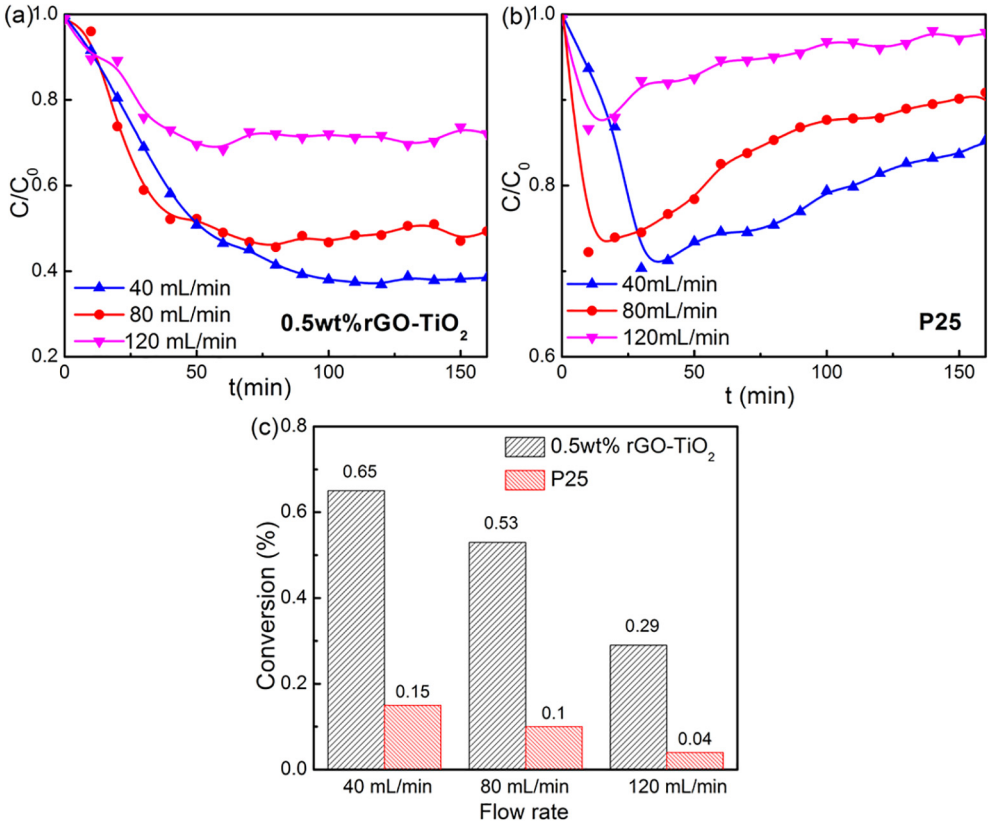

Fig. 5. Photocatalytic performances of (a) 0.5 wt% rGO-TiO_2 and (b) P25 in the degradation of gaseous o-xylene at different flow rates; (c) comparison between the removal efficiency of o-xylene by using 0.5 wt% rGO-TiO_2 and P25 at different flow rates.

factors in addition to surface area, including the pore size, surface chemical functional groups and so on. So different adsorbent exhibit different adsorptivity even with the same S_{BET} value. Previous research [59] reported that the chemical functional groups played important role in the adsorption. According to the XPS spectra (Fig. 3d), the rGO was partly reduced and there were still some residual oxygen-

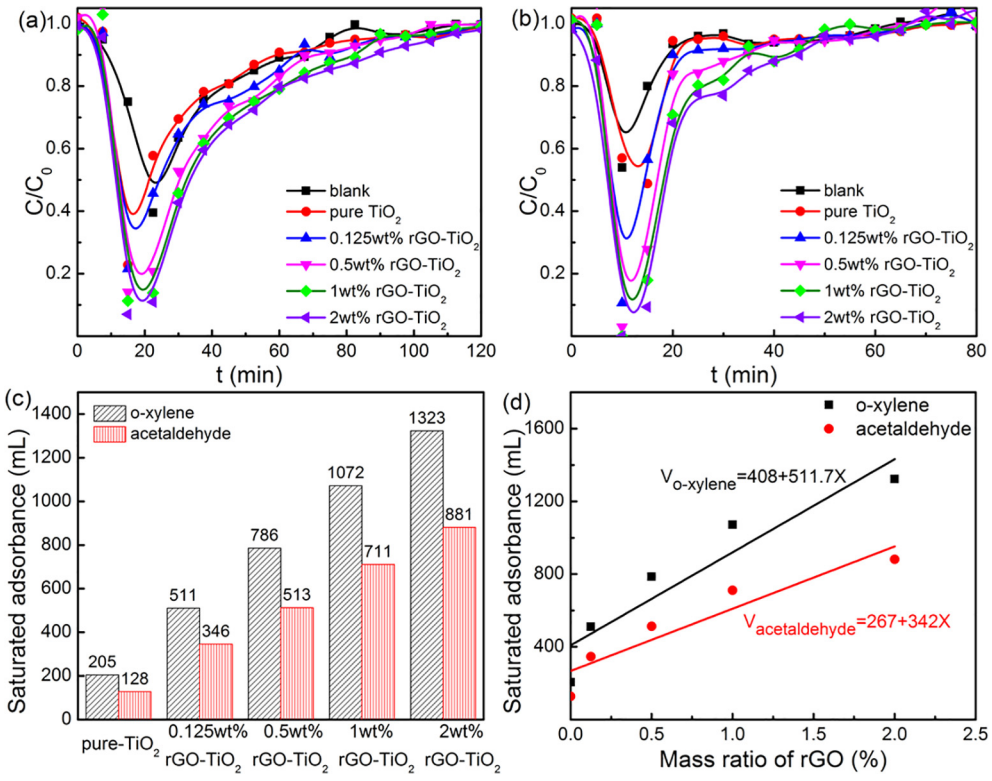

Fig. 6. Adsorption of dynamic gaseous (a) o-xylene and (b) acetaldehyde for different samples in dark condition; (c) saturated adsorbance (mL) of 0.1 g as-prepared materials for gaseous o-xylene and acetaldehyde (25 ppm); (d) relationship between the mass ratio of rGO and the saturated adsorbance (mL) of 0.1 g as-prepared materials for gaseous o-xylene and acetaldehyde. The concentration of both o-xylene and acetaldehyde was 25 ppm.

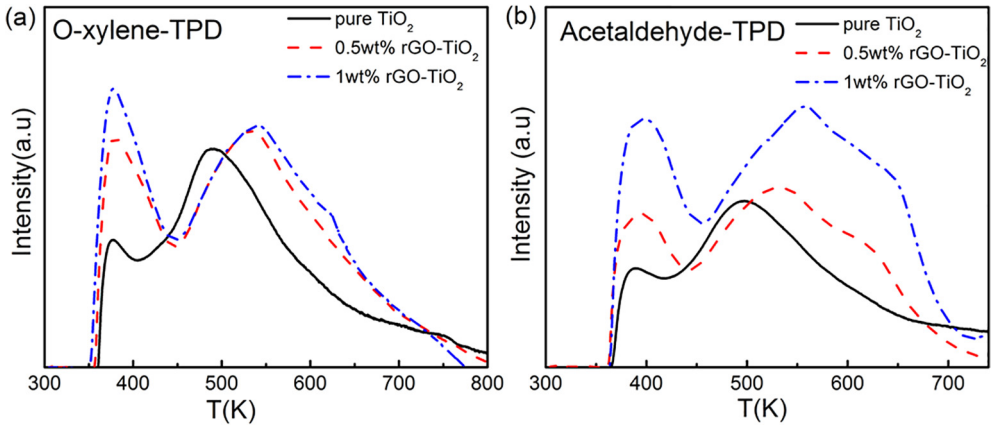

Fig. 7. (a) Desorption of o-xylene during o-xylene-TPD on the surface of different samples; (b) Desorption of acetaldehyde during acetaldehyde-TPD on the surface of different samples.

containing groups on the rGO sheet. The rGO was attached with slightly polar because of the present of oxygen-containing groups. Due to the dipole-dipole interactions between the rGO and polar acetaldehyde, the intermolecular potential energy will decrease to facilitate the adsorption. Previous report [60] has confirmed that the increase of surface concentration of oxygen-containing groups will result in higher adsorption capacity towards acetaldehyde. So it was reasonable that the nanocomposites showed enhanced adsorption capacity for acetaldehyde. Besides, o-xylene molecules will adsorbed on the π-electron rich region of rGO due to the π-π interaction, facilitating the adsorption of o-xylene. As a result, the nanocomposite showed enhanced adsoptivity for acetaldehyde and o-xylene even with a low rGO content.

The PL emission spectrum is widely accepted to characterize the trapping, immigration, and recombination of charge carriers in semiconductors. The signal quenches if the recombination of e^--h^+ pairs is inhibited. As shown in Fig. 8, the PL intensity diminished when the mass ratio of rGO increased. 2 wt% rGO-TiO_2 showed the lowest PL intensity as compared with the others. This indicates that rGO can accept photo-generated electrons from TiO_2, inhibiting the recombination of charge carriers, which is significant for the generation of free radicals.

ESR spectroscopy was used for detecting the superoxide radical ($^{\cdot}O_2^-$) and hydroxyl radicals ($^{\cdot}OH$). The quartet peaks with an intensity ratio of 1:2:2:1(Fig. 9a) are typical for the DMPO-$^{\cdot}OH$. As can be seen, the signal of DMPO-$^{\cdot}OH$ for P25 was the weakest one. In case of the hybrids, the signal intensity enhanced with the rGO content, indicating that the composite with higher rGO content can generate more $^{\cdot}OH$. In case of DMPO-$^{\cdot}O_2^-$, the signal intensity for P25 was the strongest one (Fig. 9b). In contrast to DMPO-$^{\cdot}OH$, the signal intensity decreased with decreasing rGO content, indicating a decrease in $^{\cdot}O_2^-$. This is explained as follows: it has been widely accepted that the photo-generated holes can oxidize H_2O to generate $^{\cdot}OH$, and electrons will reduce the adsorbed O_2 to generate $^{\cdot}O_2^-$ [61]. In the composite materials, a part of the photo-generated electrons that transferred from the conduction band of the TiO_2 particles to the rGO sheets got trapped by the defects in rGO sheets, which caused a decrease in electrons. In the meantime, the lifetime of holes was prolonged relatively, leading to an increase in $^{\cdot}OH$ and a decrease in $^{\cdot}O_2^-$.

To further investigate the contribution of $^{\cdot}OH$ and $^{\cdot}O_2^-$ in the oxidation process, respectively, 2,2,6,6-tetramethyl-piperi-dine-N-oxyl (TEMPO, $^{\cdot}OH$ scavenger) and p-benzoquinone ($^{\cdot}O_2^-$ scavenger) were added in as-prepared photocatalyst (0.5 wt% rGO-TiO_2). As shown in Fig. 9c, the removal efficiency of o-xylene decreased from 54% to 21% and 25% when p-benzoquinone and TEMPO was applied, respectively, indicating that $^{\cdot}O_2^-$ and $^{\cdot}OH$ played similar roles in the photocatalytic degradation process of o-xylene. In the degradation of acetaldehyde (Fig. 9d), the removal efficiency decreased from 41% to 15% and 26% when p-benzoquinone and TEMPO was applied, respectively, which suggested that $^{\cdot}O_2^-$ was the predominant radical in the degradation of acetaldehyde. As aforementioned, the amount of $^{\cdot}O_2^-$ decreased with increasing rGO content, which explain very well why the composite materials did show a clearly higher photocatalytic efficiency for the degradation of o-xylene than acetaldehyde.

3.3. Mechanism of enhanced photocatalytic activity

Based on our holistic findings on photocatalytic efficiency, structural analysis, and charge transfer as well as free radicals generation, a proper mechanism is proposed to explain the internal causes of the improvement of photocatalytic performance. As illustrated in Scheme 2, the photodegradation of gaseous pollutants can be divided into three main steps. Firstly, the gaseous pollutant molecules in the ambient atmosphere adsorb on the surface of the photocatalyst. In the meantime, electrons in the TiO_2 are excited from the valence band to the conduction band under UV light irradiation, creating e^--h^+ pairs [62]. Then, the charge carriers transfer to the molecules, including O_2 and H_2O, which were adsorbed on the surface of the photocatalyst, generating different radicals (Eq. (3)). Finally, these radicals react with the pollutants on the surfaces of the photocatalyst, leading to the final degradation of pollutants. As reported previously, the effective adsorption is the precondition for the further degradation of VOCs molecules [63–65]. However, the constant accumulation of adsorbed

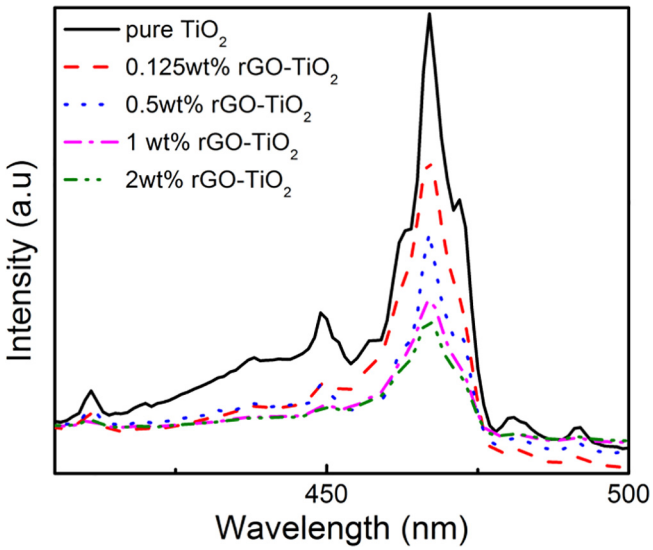

Fig. 8. PL spectra of pure TiO_2 and xwt% rGO-TiO_2.

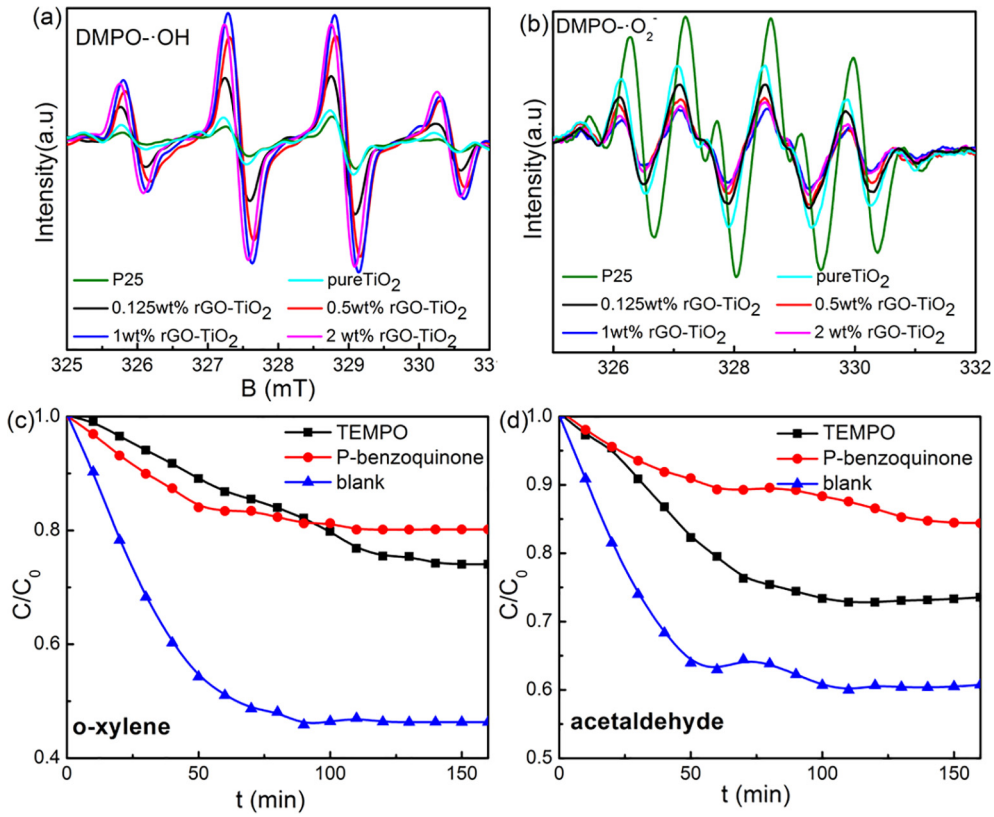

Fig. 9. ESR spectra of pure TiO_2 and as prepared nanocomposite materials under UV light irradiation in (a) aqueous dispersion and (b) methanol; photocatalytic degradation of (c) o-xylene and (d) acetaldehyde gas on 0.5 wt% rGO-TiO_2 nanocomposites with different kinds of scavengers.

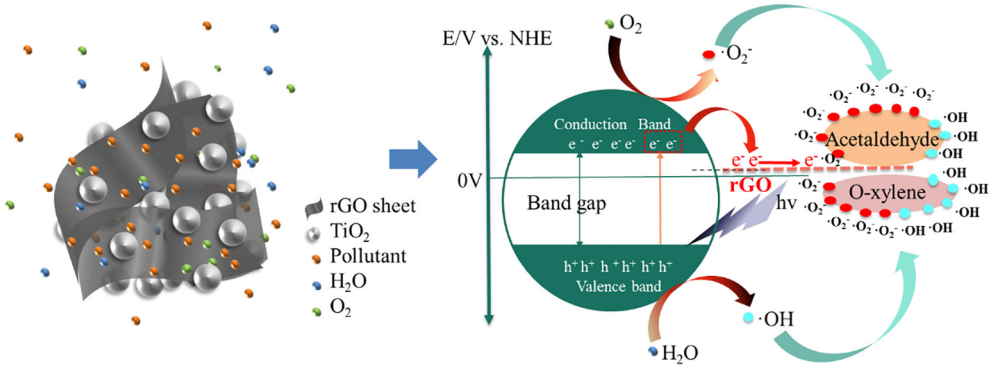

Scheme 2. Schematic structure of the rGO-TiO_2 nanocomposite and the process of photodegradation. (a) Different molecules in the ambient atmosphere adsorb on the surface of the nanocomposite. (b) Under UV light irradiation, electrons in the TiO_2 are excited to the conduction band, creating e^--h^+ pairs. Then the charge carriers transfer to O_2 and H_2O that adsorbed on the surface of the photocatalyst, generating different radicals. Finally, these radicals will react with VOCs on the surfaces of the photocatalyst and degrade them.

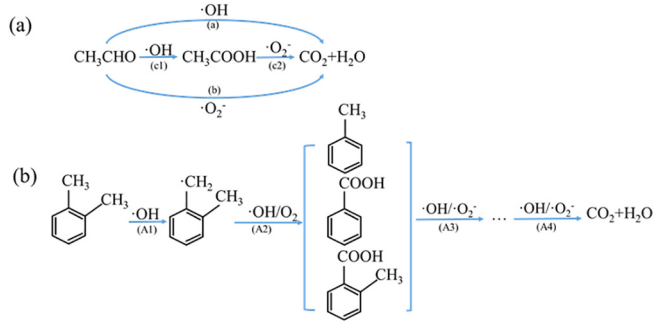

Scheme 3. Possible photodegradation mechanism of (a) acetaldehyde and (b) o-xylene.

molecules might lead to the deactivation of absorbents [5] if they cannot be degraded timely through the photocatalysis process. According to our adsorption tests (Fig. 6a and b), the adsorbed VOCs could be further decomposed into CO_2, H_2O or other intermediates after the adsorption equilibrium was reached, which kept the removal efficiency of VOCs remaining at a high level during photocatalysis process (Fig. 4a and b).

When rGO is combined with TiO_2, the specific surface area and the π-π bonds in graphene enhance the adsorptivity for organic compounds, which has been confirmed by the results of TPD and adsorption tests. Besides, the addition of rGO can facilitate the charge separation in TiO_2. According to the previous report [66], most of the charge carriers recombine and then release the energy as heat. In the composite material, the calculated work function of graphene is 4.42 eV and the conduction band position of anatase is about −4.21 eV with a band gap of 3.2 eV [67]. Thus, as confirmed by PL spectra, photo-generated electrons in TiO_2 can transfer from the conduction band of the TiO_2 nanoparticles to the rGO sheets, prolonging the lifetime of photo-generated carriers. Normally, the separated charge carriers can migrate to the surface of the photocatalyst and react with O_2, H_2O or hydroxyl groups, which adsorbed on the surfaces of TiO_2, generating $^{\cdot}OH$ and $^{\cdot}O_2^-$. However,

in the composite material, parts of the electrons were captured by the defects in the rGO sheets, prolonging the lifetime of the holes. As a result, the composite material generated more $^{\cdot}OH$ while less $^{\cdot}O_2^-$ (Eq. (4)). Holes and free radicals will react with o-xylene and acetaldehyde that adsorbed on the surfaces of the photocatalyst, leading to the final degradation.

$$H_2O + O_2 \xrightarrow[h\upsilon]{TiO_2} {}^{\cdot}OH + {}^{\cdot}O_2^- + H^+ \quad (3)$$

$$H_2O + O_2 \xrightarrow[h\upsilon]{rGO-TiO_2} {}^{\cdot}OH\ (\text{increase}) + {}^{\cdot}O_2^-\ (\text{decrease}) + H^+ \quad (4)$$

As aforementioned, as-prepared nanocomposites were efficient photocatalysts to decompose dynamical gaseous acetaldehyde and o-xylene. The improvement of photocatalytic activity was attributed to the low recombination rate of photoinduced e^--h^+ pairs and the excellent adsorptivity for pollutants, which were verified by PL spectra, TPD profiles, and adsorption tests, respectively. Excessive rGO sheets will cause the shielding effect. That is to say, rGO sheets can act as a light filter, which can weaken the light intensity that irradiating on the TiO_2 particles, limiting the utilization of the light energy. Besides, the amount of $^{\cdot}O_2^-$ decreases with increasing rGO content. These factors led to a decrease of the photocatalytic efficiency when the rGO content was higher than 0.5 wt%. Notably, the removal efficiency of acetaldehyde was higher than that of o-xylene when P25 was applied. It could be that the small formula weight of acetaldehyde makes it easier to decompose than o-xylene. After combining rGO with TiO_2, the removal efficiency of o-xylene was higher than that of acetaldehyde with identical as-prepared composite material. It mainly relates to the difference between the adsorbance and photodegradation mechanism of o-xylene and acetaldehyde. The composite material exhibits a better adsorptivity for o-xylene owing to the π-π conjugation between rGO and o-xylene. Besides, the different photodegradation mechanism may also intensify the difference between acetaldehyde and o-xylene. The possible pathways way of acetaldehyde degradation are illustrated in Scheme 3a according the previous research [18]. A part of acetaldehyde could be oxidized into carbon dioxide and water by $^{\cdot}O_2^-$ (path a) or $^{\cdot}OH$ (path b) directly. The rest could firstly be oxidized into acetic acid by $^{\cdot}OH$ (path c1), and then oxidized into carbon dioxide and water by $^{\cdot}O_2^-$ (path c2). With the addition of rGO, the amount of $^{\cdot}OH$ increased, facilitating step a and step c1. However, step b and step c2 might be suppressed since the amount of $^{\cdot}O_2^-$ decreased. The photodegradation process of o-xylene is much more complex than acetaldehyde and types of intermediates have been detected. One of the possible pathway way of o-xylene degradation is shown in Scheme 3b. The first step is the H-abstraction of the methyl group under the action of $^{\cdot}OH$ (path A1) [68]. Then it can be oxidized into toluene, formic acid or ortho-toluic acid by O_2 and $^{\cdot}OH$ (path A2) [5,69]. After that, the three above oxidation products will be further converted into a series of small molecular intermediates (path A3). Finally, these intermediates could be decomposed into carbon dioxide and water by oxidation reactions under the combined action of $^{\cdot}O_2^-$ and $^{\cdot}OH$ (path A4) [70]. With the addition of rGO, those steps relating to $^{\cdot}OH$ would be promoted, nevertheless, steps relating to $^{\cdot}O_2^-$ might be suppressed due to the changes in the amount of free radicals.

According to the degradation tests in different flow rates, the as-prepared nanocomposites showed significantly higher and more stable photocatalytic activity than P25 at a wide range of flow rates. The photocatalytic activity of P25 decreased already after 25 min, while the nanocomposites showed sustainable photodegradation during the tests (160 min). According to the previous research [5,18,68–70], kinds of intermediates were generated and adsorbed on the surface of P25 during the photodegradation process. The photocatalytic efficiency decreased since the adsorbed intermediates cannot be further oxidized timely. As-prepared nanocomposites showed stable activity during the tests since they generated more $^{\cdot}OH$ than P25. $^{\cdot}OH$ was found to be one of the main radicals for the mineralization of aromatic compounds. It can facilitate the further oxidation of intermediates that adsorbed on the active sites. As a result, the nanocomposites showed high degradation efficiency and stable activity at a wide range of flow rate.

4. Conclusion

In this work, the hybrids of rGO-TiO_2 were prepared through a facile solvothermal treatment. The composite materials exhibited enhanced adsorptivity for VOCs and prolonged lifetime of charge carriers simultaneously. As a result, as-prepared materials showed outstanding photocatalytic activity in the degradation of low concentration (at ppm level) dynamic gaseous acetaldehyde and o-xylene. Materials with optimized performance were achieved at a mass ratio of 0.5 wt%, resulting in an efficiency of 42% for the degradation of acetaldehyde and 54% for the degradation of o-xylene. For comparison, the photocatalytic efficiency of P25 photocatalyst was only 12% for acetaldehyde and 15% for o-xylene. The removal efficiency of o-xylene was higher than that of acetaldehyde with identical composite material since o-xylene and acetaldehyde showed different adsorption abilities and photodegradation mechanisms. At a wide range of different gas flow rates, the rGO-TiO_2 nanocomposites exhibited a high and stable photocatalytic activity during the whole testing procedure. Moreover, the photodegradation mechanism of acetaldehyde and o-xylene has been proposed based on the above analysis. Overall, this work explored the efficient adsorption and sustainable degradation of different types of VOCs, which will be beneficial to design the high-efficiency and ultra-stable photocatalyst materials.

Acknowledgement

This work was financially supported by the National Key Research and Development Program of China (2016YFA0203000), the International Partnership Program of Chinese Academy of Sciences (GJHZ1656) and the NSFC-DFG bilateral organization program (51761135107 and SE 2526-3/1). DS acknowledges financial support by DFG within the Cluster of Excellence “Engineering of Advanced Materials” (project EXC 315) (Bridge Funding).

Appendix A. Supplementary data

Supplementary data associated with this article can be found, in the online version, at http://dx.doi.org/10.1016/j.cej.2018.05.107.

References

[1] L.C. Fernandez, R.F. Alvarez, F.J. Gonzalez-Barcala, J.A.R. Portal, Indoor air contaminants and their impact on respiratory pathologies, Arch. Bronconeumol. 49 (2013) 22–27.
[2] N.L. Ng, J.H. Kroll, A.W.H. Chan, P.S. Chhabra, R.C. Flagan, J.H. Seinfeld, Secondary organic aerosol formation from m-xylene, toluene, and benzene, Atmos. Chem. Phys. 7 (2007) 3909–3922.
[3] X. Shen, Y. Zhao, Z. Chen, D. Huang, Heterogeneous reactions of volatile organic compounds in the atmosphere, Atmos. Environ. 68 (2013) 297–314.
[4] N. Daneshvar, D. Salari, A.R. Khataee, Photocatalytic degradation of azo dye acid red 14 in water on ZnO as an alternative catalyst to TiO_2, J. Photochem. Photobiol. A: Chem. 162 (2004) 317–322.
[5] Y. Huang, S.S. Ho, Y. Lu, R. Niu, L. Xu, J. Cao, S. Lee, Removal of indoor volatile organic compounds via photocatalytic oxidation: a short review and prospect, Molecules 21 (2016) 56.
[6] S. Wang, H.M. Ang, M.O. Tade, Volatile organic compounds in indoor environment and photocatalytic oxidation: state of the art, Environ. Int. 33 (2007) 694–705.
[7] K. Zhang, K.C. Kemp, V. Chandra, Homogeneous anchoring of TiO_2 nanoparticles on graphene sheets for waste water treatment, Mater. Lett. 81 (2012) 127–130.
[8] W.K. Jo, H.J. Kang, Polyacrylonitrile-TiO_2 fibers for control of gaseous aromatic compounds, Ind. Eng. Chem. Res. 52 (2013) 4475–4483.
[9] A.A. Assadi, J. Palau, A. Bouzaza, D. Wolbert, Modeling of a continuous photocatalytic reactor for isovaleraldehyde oxidation: effect of different operating parameters and chemical degradation pathway, Chem. Eng. Res. Des. 91 (2013) 1307–1316.
[10] A.A. Assadi, A. Bouzaza, M. Lemasle, D. Wolbert, Removal of trimethylamine and isovaleric acid from gas streams in a continuous flow surface discharge plasma reactor, Chem. Eng. Res. Des. 93 (2015) 640–651.

[11] A.A. Assadi, A. Bouzaza, S. Merabet, D. Wolbert, Modeling and simulation of VOCs removal by nonthermal plasma discharge with photocatalysis in a continuous reactor: synergetic effect and mass transfer, Chem. Eng. J. 258 (2014) 119–127.

[12] A.A. Assadi, A. Bouzaza, D. Wolbert, Photocatalytic oxidation of trimethylamine and isovaleraldehyde in an annular reactor: influence of the mass transfer and the relative humidity, J. Photochem. Photobiol. A: Chem. 236 (2012) 61–69.

[13] W. Elfallah, A.A. Assadi, A. Bouzaza, D. Wolbert, J. Kiwi, S. Rtimi, Innovative and stable TiO_2 supported catalytic surfaces removing aldehydes under UV-light irradiation, J. Photochem. Photobiol. A: Chem. 343 (2017) 96–102.

[14] A.Y. Chen, S.S. Shi, F. Liu, Y. Wang, X. Li, J.F. Gu, X.F. Xie, Effect of annealing atmosphere on the thermal coarsening of nanoporous gold films, Appl. Surf. Sci. 355 (2015) 133–138.

[15] I. Jansson, S. Suárez, F.J. Garcia-Garcia, B. Sánchez, Zeolite–TiO_2 hybrid composites for pollutant degradation in gas phase, Appl. Catal. B Environ. 178 (2015) 100–107.

[16] T. Hirakawa, P.V. Kamat, Charge separation and catalytic activity of Ag@TiO_2 core-shell composite clusters under UV-irradiation, J. Am. Chem. Soc. 127 (2005) 3928–3934.

[17] V. Subramanian, E. Wolf, P.V. Kamat, Semiconductor-metal composite nanostructures. To what extent do metal nanoparticles improve the photocatalytic activity of TiO_2 films? J. Phys. Chem. B 105 (2001) 11439–11446.

[18] Q. Zeng, X. Xie, X. Wang, Y. Wang, G. Lu, D.Y.H. Pui, J. Sun, Enhanced photocatalytic performance of Ag@TiO_2 for the gaseous acetaldehyde photodegradation under fluorescent lamp, Chem. Eng. J. 341 (2018) 83–92.

[19] Z. Liu, P. Fang, S. Wang, Y. Gao, F. Chen, F. Zheng, Y. Liu, Y. Dai, Photocatalytic degradation of gaseous benzene with CdS-sensitized TiO_2 film coated on fiberglass cloth, J Mol. Catal. A-Chem. 363–364 (2012) 159–165.

[20] M. Gholami, H.R. Nassehinia, A. Jonidijafari, S. Nasseri, A. Esrafili, Comparison of Benzene & Toluene removal from synthetic polluted air with use of Nano photocatalytic TiO_2/ZnO process, J Environ. Health Sci. 12 (2014) 1–8.

[21] J.Y. Lee, W.K. Jo, Heterojunction-based two-dimensional N-doped TiO_2/WO_3 composite architectures for photocatalytic treatment of hazardous organic vapor, J. Hazard. Mater. 314 (2016) 22–31.

[22] R. Khan, T.J. Kim, Preparation and application of visible-light-responsive Ni-doped and SnO_2-coupled TiO_2 nanocomposite photocatalysts, J. Hazard. Mater. 163 (2009) 1179–1184.

[23] F. Fresno, M.D. Hernández-Alonso, D. Tudela, J.M. Coronado, J. Soria, Photocatalytic degradation of toluene over doped and coupled (Ti, M)O_2 (M = Sn or Zr) nanocrystalline oxides: influence of the heteroatom distribution on deactivation, Appl. Catal. B Environ. 84 (2008) 598–606.

[24] C. Feng, X. Huang, Y. Wang, M. Sun, D. Li, Visible light photocatalytic behavior of manganese carbonate/titanium dioxide nanocomposites based on photoinduced interfacial charge transfer, Mater. Lett. 155 (2015) 23–26.

[25] J. Wang, R. Hong, W. Li, D. Li, Y. Hu, J. Chen, Y. Shao, Y. Zheng, Highly efficient oxidation of gaseous benzene on novel Ag_3VO_4/TiO_2 nanocomposite photocatalysts under visible and simulated solar light irradiation, J. Phys. Chem. C 116 (2012) 13935–13943.

[26] A.J. Maira, J.M. Coronado, V. Augugliaro, K.L. Yeung, J.C. Conesa, J. Soria, Fourier transform infrared study of the performance of nanostructured TiO_2 particles for the photocatalytic oxidation of gaseous toluene, J. Catal. 202 (2001) 413–420.

[27] A.H. Mamaghani, F. Haghighat, C.S. Lee, Photocatalytic oxidation technology for indoor environment air purification: the state-of-the-art, Appl. Catal. B Environ. 203 (2017) 247–269.

[28] J. Mo, Y. Zhang, Q. Xu, Y. Zhu, J.J. Lamson, R. Zhao, Determination and risk assessment of by-products resulting from photocatalytic oxidation of toluene, Appl. Catal. B Environ. 89 (2009) 570–576.

[29] C.H. Ao, S.C. Lee, Enhancement effect of TiO_2 immobilized on activated carbon filter for the photodegradation of pollutants at typical indoor air level, Appl. Catal. B Environ. 44 (2003) 191–205.

[30] L. Cao, Z. Gao, S.L. Suib, T.N. Obee, S.O. Hay, J.D. Freihaut, Photocatalytic oxidation of toluene on nanoscale TiO_2 catalysts: studies of deactivation and regeneration, J. Catal. 196 (2000) 253–261.

[31] W. Wang, J. Yu, Q. Xiang, B. Cheng, Enhanced photocatalytic activity of hierarchical macro/mesoporous TiO_2–graphene composites for photodegradation of acetone in air, Appl. Catal. B Environ. 119–120 (2012) 109–116.

[32] D. Zhao, G. Sheng, C. Chen, X. Wang, Enhanced photocatalytic degradation of methylene blue under visible irradiation on graphene@TiO_2 dyade structure, Appl. Catal. B Environ. 111–112 (2012) 303–308.

[33] J. Liu, L. Liu, H. Bai, Y. Wang, D.D. Sun, Gram-scale production of graphene oxide–TiO_2 nanorod composites: towards high-activity photocatalytic materials, Appl. Catal. B Environ. 106 (2011) 76–82.

[34] L.I. Chun-Zhong, T. Jun, S.U.N. Xiu-Li, C. Ai-Ping, L.V. Hui, Synthesis of graphene/Ni/TiO_2/CNTs composites and photocatalytic activities, J. Inorg. Mater. 29 (2014) 1061–1066.

[35] L.I. Ting-Ting, D. Qi-Zheng, Y. Xuan, Y. Zhi-Zhong, J.I.N. Hai-Ze, L.I. Cui-Xia, Preparation and photocatalytic properties of mesoporous RGO/TiO_2; composites, J. Inorg. Mater. 32 (2017) 357–364.

[36] Q. Huang, S. Tian, D. Zeng, X. Wang, W. Song, Y. Li, W. Xiao, C. Xie, Enhanced photocatalytic activity of chemically bonded TiO_2/graphene composites based on the effective interfacial charge transfer through the C-Ti bond, ACS Catal. 3 (2013) 1477–1485.

[37] J.S. Lee, K.H. You, C.B. Park, Highly photoactive, low bandgap TiO_2 nanoparticles wrapped by graphene, Adv. Mater. 24 (2012) 1084–1088.

[38] C. Xu, J. Zhu, R. Yuan, X. Fu, More effective use of graphene in photocatalysis by conformal attachment of small sheets to TiO_2 spheres, Carbon 96 (2016) 394–402.

[39] M. Sohail, H. Xue, Q. Jiao, H. Li, K. Khan, S. Wang, Y. Zhao, Synthesis of well-dispersed TiO_2@reduced graphene oxide (rGO) nanocomposites and their photocatalytic properties, Mater. Res. Bull. 90 (2017) 125–130.

[40] H. Atout, M.G. Álvarez, D. Chebli, A. Bouguettoucha, D. Tichit, J. Llorca, F. Medina, Enhanced photocatalytic degradation of methylene blue: preparation of TiO_2/reduced graphene oxide nanocomposites by direct sol-gel and hydrothermal methods, Mater. Res. Bull. 95 (2017) 578–587.

[41] E. Vasilaki, I. Georgaki, D. Vernardou, M. Vamvakaki, N. Katsarakis, Ag-loaded TiO_2/reduced graphene oxide nanocomposites for enhanced visible-light photocatalytic activity, Appl. Surf. Sci. 353 (2015) 865–872.

[42] D. Liang, C. Cui, H. Hu, Y. Wang, S. Xu, B. Ying, P. Li, B. Lu, H. Shen, One-step hydrothermal synthesis of anatase TiO_2/reduced graphene oxide nanocomposites with enhanced photocatalytic activity, J. Alloy. Compd. 582 (2014) 236–240.

[43] L. Luo, Y. Yang, A. Zhang, M. Wang, Y. Liu, L. Bian, F. Jiang, X. Pan, Hydrothermal synthesis of fluorinated anatase TiO_2/reduced graphene oxide nanocomposites and their photocatalytic degradation of bisphenol A, Appl. Surf. Sci. 353 (2015) 469–479.

[44] A.W. Morawski, E. Kusiak-Nejman, A. Wanag, J. Kapica-Kozar, R.J. Wróbel, B. Ohtani, M. Aksienionek, L. Lipińska, Photocatalytic degradation of acetic acid in the presence of visible light-active TiO_2 -reduced graphene oxide photocatalysts, Catal. Today 280 (2017) 108–113.

[45] S.D. Perera, R.G. Mariano, K. Vu, N. Nour, O. Seitz, Y. Chabal, K.J. Balkus, Hydrothermal synthesis of graphene-TiO_2 nanotube composites with enhanced photocatalytic activity, ACS Catal. 2 (2012) 949–956.

[46] P. Wang, J. Wang, X. Wang, H. Yu, J. Yu, M. Lei, Y. Wang, One-step synthesis of easy-recycling TiO_2-rGO nanocomposite photocatalysts with enhanced photocatalytic activity, Appl. Catal. B Environ. 132–133 (2013) 452–459.

[47] Y. Zhang, N. Zhang, Z.R. Tang, Y.J. Xu, Improving the photocatalytic performance of graphene-TiO_2 nanocomposites via a combined strategy of decreasing defects of graphene and increasing interfacial contact, PCCP 14 (2012) 9167–9175.

[48] X.Y. Lu, X.F. Xie, J.Q. Luo, J. Sun, Cesium-doped graphene grown in situ with ultrasmall TiO_2 nanoparticles for high-performance lithium-ion batteries, New J. Chem. 41 (2017) 7938–7946.

[49] W.S. Hummers, R.E. Offeman, Preparation of graphitic oxide, J. Am. Chem. Soc. 80 (1958) 1339–1339.

[50] C.H. Xu, J. Sun, L. Gao, Direct growth of monodisperse SnO_2 nanorods on graphene as high capacity anode materials for lithium ion batteries, J. Mater. Chem. 22 (2012) 975–979.

[51] H. Zhang, X.J. Lv, Y.M. Li, Y. Wang, J.H. Li, P25-graphene composite as a high performance photocatalyst, ACS Nano 4 (2010) 380–386.

[52] R. Rao, R. Podila, R. Tsuchikawa, J. Katoch, D. Tishler, A.M. Rao, M. Ishigami, Effects of layer stacking on the combination Raman modes in graphene, ACS Nano 5 (2011) 1594–1599.

[53] K.N. Kudin, B. Ozbas, H.C. Schniepp, R.K. Prud'homme, I.A. Aksay, R. Car, Raman spectra of graphite oxide and functionalized graphene sheets, Nano Lett. 8 (2008) 36–41.

[54] Y.H. Ding, P. Zhang, Q. Zhuo, H.M. Ren, Z.M. Yang, Y. Jiang, A green approach to the synthesis of reduced graphene oxide nanosheets under UV irradiation, Nanotechnology 22 (2011) 215601.

[55] C. Nethravathi, M. Rajamathi, Chemically modified graphene sheets produced by the solvothermal reduction of colloidal dispersions of graphite oxide, Carbon 46 (2008) 1994–1998.

[56] L.G. Cançado, K. Takai, T. Enoki, M. Endo, Y.A. Kim, H. Mizusaki, A. Jorio, L.N. Coelho, R. Magalhães-Paniago, M.A. Pimenta, General equation for the determination of the crystallite size La of nanographite by Raman spectroscopy, Appl. Phys. Lett. 88 (2006) 163106.

[57] Y. Matsumoto, M. Koinuma, S.Y. Kim, Y. Watanabe, T. Taniguchi, K. Hatakeyama, H. Tateishi, S. Ida, Simple photoreduction of graphene oxide nanosheet under mild conditions, ACS Appl. Mater. Inter. 2 (2010) 3461–3466.

[58] L.W. Zhang, H.-B. Fu, Y.-F. Zhu, Efficient TiO_2 photocatalysts from surface hybridization of TiO_2 particles with graphite-like carbon, Adv. Funct. Mater. 18 (2008) 2180–2189.

[59] X. Zhang, B. Gao, A.E. Creamer, C. Cao, Y. Li, Adsorption of VOCs onto engineered carbon materials: a review, J. Hazard. Mater. 338 (2017) 102–123.

[60] K.J. Kim, C.S. Kang, Y.J. You, M.C. Chung, M.W. Woo, W.J. Jeong, N.C. Park, H.G. Ahn, Adsorption–desorption characteristics of VOCs over impregnated activated carbons, Catal. Today 111 (2006) 223–228.

[61] C.J. Rhodes, The role of ESR spectroscopy in advancing catalytic science: some recent developments, Prog. React. Kinet. Mec. 40 (2015) 201–248.

[62] M.Y. Wang, J. Ioccozia, L. Sun, C.J. Lin, Z.Q. Lin, Inorganic-modified semiconductor TiO_2 nanotube arrays for photocatalysis, Energy Environ. Sci. 7 (2014) 2182–2202.

[63] H.S. Taylor, A Theory of the Catalytic Surface, Proc. R. Soc. London 108 (1925) 105–111.

[64] H. Yoneyama, T. Torimoto, Titanium dioxide/adsorbent hybrid photocatalysts for photodestruction of organic substances of dilute concentrations, Catal. Today 58 (2000) 133–140.

[65] J. Yang, D. Chen, Y. Zhu, Y. Zhang, Y. Zhu, 3D–3D porous Bi_2WO_6/graphene hydrogel composite with excellent synergistic effect of adsorption-enrichment and photocatalytic degradation, Appl. Catal. B Environ. 205 (2016).

[66] T. Hisatomi, J. Kubota, K. Domen, Recent advances in semiconductors for photocatalytic and photoelectrochemical water splitting, Chem. Soc. Rev. 43 (2014) 7520–7535.

[67] J. Zhang, Z. Xiong, X.S. Zhao, Graphene–metal–oxide composites for the degradation of dyes under visible light irradiation, J. Mater. Chem. 21 (2011) 3634.

[68] M.M. Ameen, G.B. Raupp, Reversible catalyst deactivation in the photocatalytic oxidation of dilute o-xylene in air, J. Catal. 184 (1999) 112–122.

[69] C.C. Pei, W.F. Leung, Photocatalytic oxidation of nitrogen monoxide and o-xylene by TiO_2/ZnO/Bi_2O_3 nanofibers: optimization, kinetic modeling and mechanisms, Appl. Catal. B Environ. 174–175 (2015) 515–525.

[70] M. Sleiman, P. Conchon, C. Ferronato, J.M. Chovelon, Photocatalytic oxidation of toluene at indoor air levels (ppbv): towards a better assessment of conversion, reaction intermediates and mineralization, Appl. Catal. B Environ. 86 (2009) 159–165.